

A non-collocated method to quantify plastic deformation caused by impact pile driving

Meijers, P. C.; Tsouvalas, A.; Metrikine, A. V.

DOI

[10.1016/j.ijmecsci.2018.08.013](https://doi.org/10.1016/j.ijmecsci.2018.08.013)

Publication date

2018

Document Version

Accepted author manuscript

Published in

International Journal of Mechanical Sciences

Citation (APA)

Meijers, P. C., Tsouvalas, A., & Metrikine, A. V. (2018). A non-collocated method to quantify plastic deformation caused by impact pile driving. *International Journal of Mechanical Sciences*, 148, 1-8. <https://doi.org/10.1016/j.ijmecsci.2018.08.013>

Important note

To cite this publication, please use the final published version (if applicable). Please check the document version above.

Copyright

Other than for strictly personal use, it is not permitted to download, forward or distribute the text or part of it, without the consent of the author(s) and/or copyright holder(s), unless the work is under an open content license such as Creative Commons.

Takedown policy

Please contact us and provide details if you believe this document breaches copyrights. We will remove access to the work immediately and investigate your claim.

A Non-Collocated Method to Quantify Plastic Deformation Caused by Impact Pile Driving

P.C. Meijers^{a,*}, A. Tsouvalas^a, A.V. Metrikine^a

^a*Delft University of Technology, Faculty of Civil Engineering, Stevinweg 1, 2628CN Delft,
The Netherlands*

Abstract

The use of bolted connections between the tower and a support structure of an offshore wind turbine has created the need for a method to detect whether a monopile foundation plastically deforms during the installation procedure. Small permanent deformations are undesirable, not only because they can accelerate fatigue of the structure; but also because they can lead to misalignment between the tower and the foundation. Since direct measurements at the pile head are difficult to perform, a method based on non-collocated strain measurements is highly desirable. This paper proposes such a method. First, a physically non-linear one-dimensional model is proposed, which accounts for wave dispersion, effects that are relevant for large-diameter piles currently used by the industry. The proposed model, combined with an energy balance principle, gives an upper bound for the amount of plastic deformation caused by an impact load based on simple strain measurements. This is verified by a lab-scale experiment with a uni-axial stress state. Second, measurement data collected during pile driving of a large-diameter pile show that the proposed one-dimensional model, while able to predict the peak stresses, fails to accurately predict the full time history of the measured stress state. In contrast, an advanced model based on shell membrane theory is able to do that, showing that a bi-axial stress state is needed for these type of structures. This requires an extension of the theory for plasticity quantification presented in this paper.

*Corresponding author
Email address: p.c.meijers@tudelft.nl (P.C. Meijers)

1. Introduction

Steel monopiles are widely used in the offshore industry as a foundation structure for wind turbines. As a result of the rapid growth of the offshore wind market over the past decades, monopiles now range up to eight meters in diameter in order to support the latest generation of wind turbines [1]. Currently, hydraulic impact hammers are the preferred choice to drive these thin-walled cylindrical structures into the seabed. Each hammer blow generates a compressive stress wave, which propagates down the pile; the latter helps the pile to progress into the seabed. To overcome the increasing soil resistance at greater penetration depths, the input energy of the hammer is increased accordingly. For high energy impacts, the amplitude of the induced stress waves can cause stresses close to the yield limit of the material, increasing the risk of plastic deformations at the pile head.

Until recently, these permanent deformations were of little concern, since the pile head did not contribute to the bearing capacity of the pile due to the use of a grouted connection between the monopile and the superstructure. However, to reduce the cost of offshore wind energy, bolted connections have become more popular in recent years, since they require less steel [1]. This type of connection asks for a perfect alignment between the pile head and the superstructure; and any plastic deformation of the pile head can potentially disturb this delicate alignment. Furthermore, plastic deformation is unfavourable for the remaining service life of the whole structure, since it fatigues the material. A method to infer whether plastic deformation has occurred is therefore needed.

The high stresses generated by a hammer blow can cause damage not only to the pile itself, but also to the sensors, making strain or acceleration measurements directly at the pile head unfeasible during the pile process. A workable method should thus rely on non-collocated measurements, i.e. measurements at another location than where the plastic deformation occurs. Fortunately, it

is current practice to monitor the stress levels in the pile during installation.
30 From these measurements, which are taken a few meters below the pile head,
and with a wave propagation model similar to the one proposed by Smith [2],
the pile driving process is monitored [3]. Smith’s model is based on the classical
one-dimensional wave equation, which is non-dispersive. Due to its low compu-
tational cost, it is widely used in industry, even though more advanced models
35 have been developed over the years; each model addresses different aspects of
pile driving, e.g. sound radiation [4, 5], and soil modelling [6].

To quantify plastic deformation at the pile head from non-collocated mea-
surements, this paper augments the one-dimensional model of the pile installa-
tion process with two features: wave dispersion caused by the geometry of the
40 structure and non-linear material behaviour. The former is needed to correctly
model the stress wave propagation in the pile, since dispersion cannot be ne-
glected for large-diameter monopiles [7]. The latter is included to account for
the physical non-linearity that is necessary to quantify plasticity.

The propagation of elasto-plastic stress waves in solid metal cylinders has
45 been studied already from the 1940s onwards; validated against high velocity
impact experiments, rate-independent theories based on the classical wave equa-
tion were developed [8, 9]. More advanced models included lateral inertia of the
cross-section [10] and rate-dependency of the material [11]. Using these models,
the dynamic properties of metals can be determined from experimental data
50 [12]. More recently, an energy-based approach to study these impact tests was
reported [13].

Similar axial impact tests have been performed on hollow cylindrical shells
[14, 15]. These thin-walled structures are used in the automotive industry as
energy absorption devices, since the dynamic buckling of the cylinders remove
55 energy from the system. Lepik [16] and Karagiozova et al. [17, 18] showed that
the type of dynamic buckling and thus the deformed state of the cylinder after
impact depends on the axial stress wave propagation. Moreover, Karagiozova et
al. [19] reported that for low-velocity (drop hammer) impacts, which resemble
impact pile driving, most of the permanent deformation is concentrated in a

60 small region at the impacted end of the cylinder. However, the use of non-
collocated strain sensors mounted on the structure itself to quantify the amount
of plastic deformation during the pile driving process, as proposed in this paper,
has not been found in literature so far.

By eliminating terms from a shell theory based on justified assumptions,
65 Section 2 derives the governing equations for elasto-plastic waves propagating
in a monopile, resulting in a more accurate description of the behaviour of these
waves, which is also valid for the large-diameter monopiles currently used by the
offshore wind industry. Subsequently, Section 3 proposes a method to quantify
plastic deformation based on non-collocated strain measurements and an energy
70 balance. The proposed method is then validated against two experiments: Sec-
tion 4 presents a lab-scale experiment of a copper bullet hitting a solid rod [12],
and Section 5 discusses a full-scale experiment of a foundation pile installed for
offshore wind. The former experiment allows one to validate the concept of the
energy balance in a well controlled environment. The latter experiment allows
75 one to validate the wave propagation model including wave dispersion effects in
a more realistic setting. Finally, conclusions are drawn in Section 6. The authors
believe that these two amendments to the classical model of Smith [2] set the
basis for the next generation models to be included in studies of the drivability
of piles and detection of plastic deformation for offshore wind applications.

80 **2. Governing equations**

A schematic representation of the pile-hammer-soil system is shown in Fig-
ure 1, together with the chosen cylindrical coordinate system that is used
throughout this paper; the axial, tangential, and radial direction are denoted
by x , θ and r , respectively. The monopile has outer radius R , wall thickness
85 h , and length L . In the next section, strain levels for the detection method
will be considered at the cross-section located at $x = a$. First, different models
describing the propagation of elastic waves are compared to correctly capture
the effect of wave dispersion. Second, material non-linearity is included in order

to quantify plasticity.

90 *2.1. Governing equations for axially symmetric deformations of a cylindrically symmetric shell*

The natural starting point for deriving the governing equations is a thin cylindrical shell theory, which is justified by the assumption that the pile’s radius and length, and the excited wavelengths in the structure due to impact 95 piling are large compared to the wall thickness.

By comparing exact theory and approximate thin shell theory, Greenspon showed that the latter is adequate for predicting the dynamical characteristics of a cylindrical shell structure with a diameter to wall thickness ratio comparable to that of a monopile [20]. Although there are many thin shell theories—each 100 with their own complexity and range of applicability—they can be written in the operator form presented by Leissa [21]:

$$(\mathcal{L}_{D-M} + \beta \mathcal{L}_{\text{mod}}) \bar{\mathbf{u}} = \mathbf{0}. \quad (1)$$

In this expression, $\bar{\mathbf{u}}$ is a vector containing the three displacement components $\bar{u}, \bar{v}, \bar{w}$: the axial, tangential, and radial displacements, respectively, which are all functions of x, θ , and t . To make them dimensionless, each component is 105 divided by the radius, e.g. $\bar{u} = u/R$; bars indicate a non-dimensional quantity. The Donnell-Mushtari operator, \mathcal{L}_{D-M} , is the basis for all theories; other theories emerge by adding the modification operator \mathcal{L}_{mod} . The thickness over radius ratio $\beta \equiv h^2/12R^2$ determines the influence of this additional operator on the resulting theory. For a monopile, this ratio is much smaller than one, and the 110 frequencies of interest are relatively low. Thus, the modification term can be discarded at this point.

The nine components of the Donnell-Mushtari operator can be found in [21]. Since the wave propagation caused by the hammer forcing is assumed to be purely symmetric, the operator can be further simplified. By setting all tangential derivatives to zero, i.e. $\frac{\partial(\cdot)}{\partial\theta} = 0$, the components of the axi-symmetric

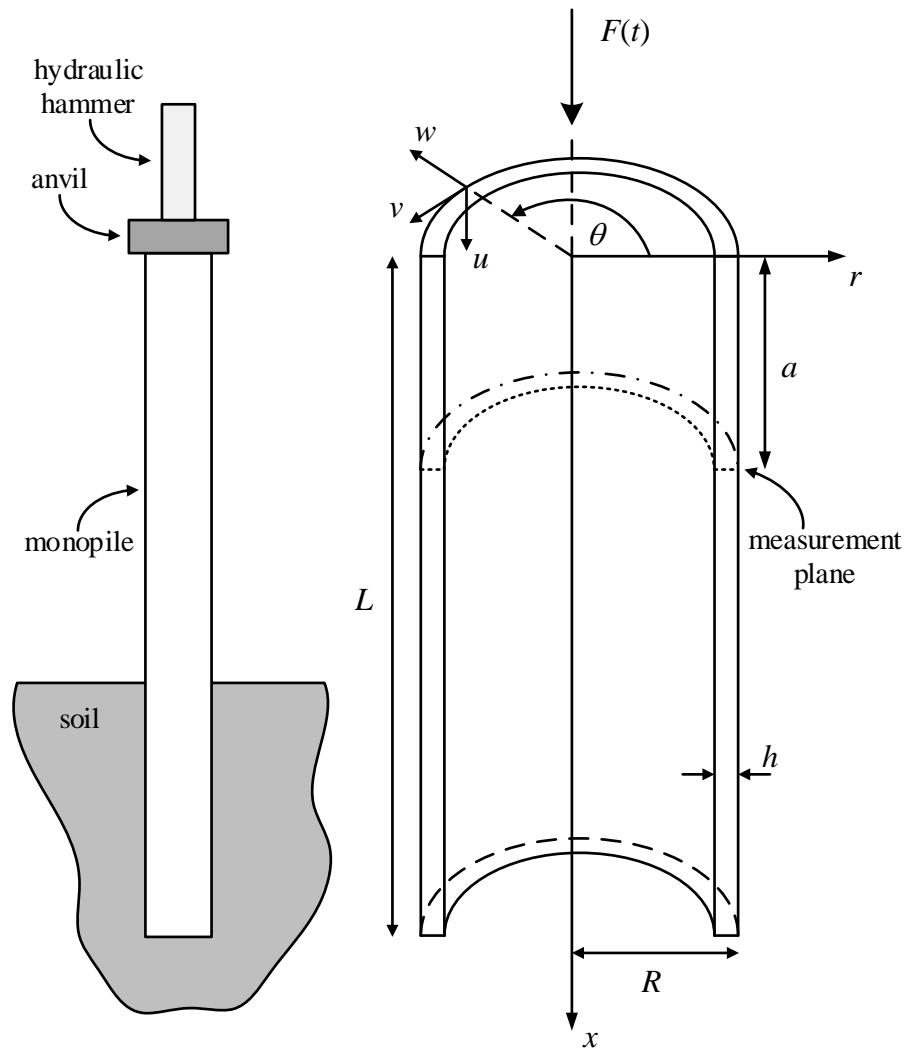


Figure 1: Left, schematic of the pile-hammer-soil system; right, overview of the thin-walled cylindrical shell structure used to derive the governing equations.

operator \mathcal{L}_{axi} yield

$$\mathcal{L}_{\text{axi}}^{11} = \frac{\partial^2}{\partial s^2} - \frac{\partial^2}{\partial \tau^2}, \quad (2a)$$

$$\mathcal{L}_{\text{axi}}^{12} = \mathcal{L}_{\text{axi}}^{21} = 0, \quad (2b)$$

$$\mathcal{L}_{\text{axi}}^{13} = \mathcal{L}_{\text{axi}}^{31} = \nu \frac{\partial}{\partial s}, \quad (2c)$$

$$\mathcal{L}_{\text{axi}}^{22} = \frac{1-\nu}{2} \frac{\partial^2}{\partial s^2} - \frac{\partial^2}{\partial \tau^2}, \quad (2d)$$

$$\mathcal{L}_{\text{axi}}^{23} = \mathcal{L}_{\text{axi}}^{32} = 0, \quad (2e)$$

$$\mathcal{L}_{\text{axi}}^{33} = 1 + \beta \frac{\partial^4}{\partial s^4} + \frac{\partial^2}{\partial \tau^2}. \quad (2f)$$

The off-diagonal zeros in this operator, e.g. $\mathcal{L}_{\text{axi}}^{12} = 0$, indicate that the torsional motions are now uncoupled from the radial and axial motions. Since the axial motions are of the major importance for pile driving, the two coupled equations are combined by eliminating the radial displacement, resulting in

$$\frac{\partial^4 \bar{u}}{\partial \tau^4} + \frac{\partial^2 \bar{u}}{\partial \tau^2} - \frac{\partial^4 \bar{u}}{\partial s^2 \partial \tau^2} - (1-\nu^2) \frac{\partial^2 \bar{u}}{\partial s^2} + \beta \left(\frac{\partial^4 \bar{u}}{\partial s^4} + \frac{\partial^6 \bar{u}}{\partial s^4 \partial \tau^2} \right) = 0. \quad (3)$$

In the above expressions, the non-dimensional axial coordinate is defined as $s = x/R$, and the dimensionless time is $\tau = \omega_r t$, with

$$\omega_r = c_p/R$$

the ring frequency. At this frequency, the breathing resonance of a ring with that radius occurs [22]. The plate velocity is

$$c_p = \sqrt{\frac{E}{\rho(1-\nu^2)}},$$

and it contains the linear elastic material properties: Young's modulus E , Poisson's ratio ν , and density ρ . Eq. (3) can be further simplified by analysing the effect of the higher-order derivatives on the dispersion characteristics as

115 discussed below.

2.2. Dispersion characteristics of cylindrical shells

The dispersion characteristics of the governing equation are expressed in terms of the dimensionless frequency $\Omega = \omega/\omega_r$ and the dimensionless wavenum-

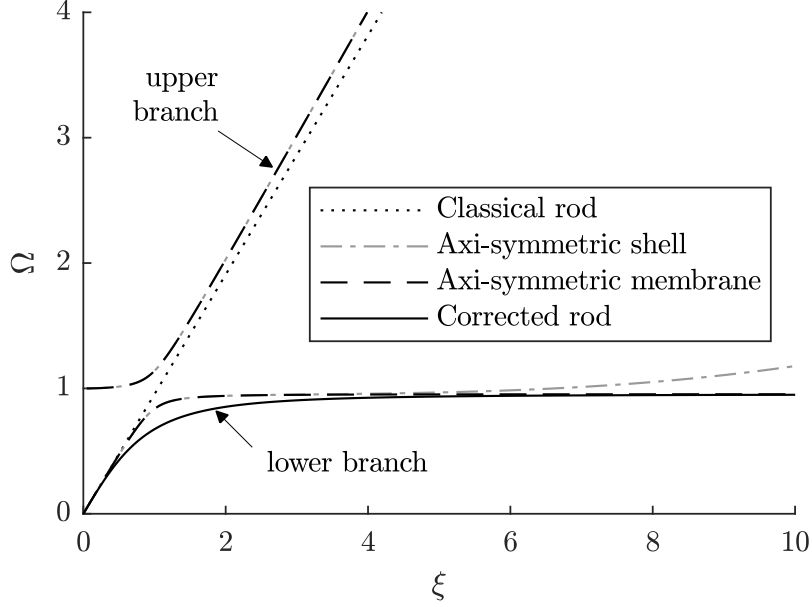


Figure 2: Dispersion curves for the considered theories computed with $\nu = 0.3$ and $\beta = 4.80 \cdot 10^{-5}$.

ber $\xi = kR$. In these expressions, ω and k designate the frequency and wavenumber, respectively. Each further simplification of the equation of motion restricts the range of applicability in terms of these dimensionless quantities. Figure 2 shows the dispersion curves, which are computed with common values for steel monopiles: $\nu = 0.3$ and $\beta = 4.80 \cdot 10^{-5}$.

As a result of the fourth-order time derivative, the dispersion curve of the axi-symmetric shell, Eq. (3), has two branches. For ξ close to zero, i.e. large wavelengths, structural motions are mainly axial, since tangential motions counteract any radial motion. However, when the ring frequency ($\Omega = 1$) is approached, the tangential component disappears, since the energy needed for in-surface shearing decreases. As a result, radial motions start to dominate [23]. When the wavenumber increases even further, axial bending energy eventually dominates the dispersion characteristics, causing the curve to bend back towards the infinite flat plate curve [22].

Given that the lower branch only bends slightly upward in the frequency range of interest, the first simplification is to neglect the bending behaviour in the shell theory. By discarding the β -terms in the shell equations, an axi-symmetric membrane theory emerges:

$$\frac{\partial^4 \bar{u}}{\partial \tau^4} + \frac{\partial^2 \bar{u}}{\partial \tau^2} - \frac{\partial^4 \bar{u}}{\partial s^2 \partial \tau^2} - (1 - \nu^2) \frac{\partial^2 \bar{u}}{\partial s^2} = 0. \quad (4)$$

As a result of this simplification, the motions in the structure are assumed to be inextensional. The two branches of the dispersion relation of the membrane theory are indistinguishable from the shell theory for $0 \leq \xi \leq 6$. The axi-symmetric membrane theory is thus a good approximation of the shell theory for small wavenumbers. This observation holds for a wider selection of properties than the ones considered in this paper.

Since the second branch only appears at frequencies above the ring frequency, an approximation of the lower branch would suffice to describe wave propagation in a monopile for waves that contain frequencies below this critical value, i.e. $\Omega = 1$. One obtains this approximation by omitting the fourth-order time derivate in the shell membrane equations, Eq. (4), resulting in

$$\frac{\partial^2 \bar{u}}{\partial \tau^2} - \frac{\partial^4 \bar{u}}{\partial s^2 \partial \tau^2} - (1 - \nu^2) \frac{\partial^2 \bar{u}}{\partial s^2} = 0. \quad (5)$$

Since higher frequencies cannot propagate in this approximate theory, its range of applicability is limited to $0 \leq \xi \leq 6$ and $0 \leq \Omega < 1 - \nu^2$. This expression for the approximate lower branch resembles the Rayleigh-Love rod theory, see [24], although the coefficient of the mixed time-space derivative is adjusted here to approach the exact dispersion curves obtained with the shell theory. Therefore, this approximate theory is referred to as the corrected rod theory from here on.

As a reference, Figure 2 also shows the dispersion curve for the classic non-dispersive rod theory, which is the basis for Smith's pile driving model [2] commonly used in practice. The equation of motion in this case simplifies further to

$$\frac{\partial^2 \bar{u}}{\partial \tau^2} - (1 - \nu^2) \frac{\partial^2 \bar{u}}{\partial s^2} = 0. \quad (6)$$

For low frequencies and wavenumbers ($0 \leq \xi \lesssim 0.5$ and $0 \leq \Omega \lesssim 0.5$), the lower branch of the axi-symmetric shell theories coincides with the one obtained from the non-dispersive theory, showing the validity of Smith's pile driving model when the frequency content of the hammer forcing is well below the ring frequency. However, when the forcing contains frequencies around the ring frequency, the effect of stress wave dispersion can no longer be neglected. This simple fact is very often overlooked in practice.

2.3. Inclusion of physical non-linearity

So far, all presented expressions are derived on the basis of a linear elastic constitutive law. To incorporate plastic deformations, the stress components of the plane stress state of the axi-symmetric membrane theory, Eq. (4), are considered. By dividing each component by the Young's modulus E , the dimensionless version of the stress tensor is obtained, i.e.

$$(1 - \nu^2) \bar{\sigma}_s = \frac{\partial \bar{u}}{\partial s} + \nu \bar{w}, \quad (7a)$$

$$(1 - \nu^2) \bar{\sigma}_\theta = \bar{w} + \nu \frac{\partial \bar{u}}{\partial s}, \quad (7b)$$

$$(1 - \nu^2) \bar{\sigma}_{s\theta} = \frac{1}{2} \frac{\partial \bar{v}}{\partial s} = 0, \quad (7c)$$

in which $\bar{\sigma}_s$, $\bar{\sigma}_\theta$ and $\bar{\sigma}_{s\theta}$ are the axial, hoop and membrane shear stress, respectively. The shear stress vanishes due to the assumption that the pile driving process causes no torsional motions in the structure, leaving only two non-zero stress components.

The relative importance of these components is frequency dependent. By expressing the displacements in Eq. (7) in terms of the dimensionless frequency and wavenumber, the ratio between the axial and the hoop stress is

$$\frac{\bar{\sigma}_s}{\bar{\sigma}_\theta} = \frac{\Omega^2 - (1 - \nu^2)}{\nu \Omega^2}. \quad (8)$$

Figure 3 shows a graph of this ratio for $\nu = 0.3$ as a function of the dimensionless frequency. Since $\bar{\sigma}_s/\bar{\sigma}_\theta$ tends to minus infinity when Ω approaches zero, the axial stress dominates the hoop stress for low frequencies ($\Omega < 0.5$). Therefore, it

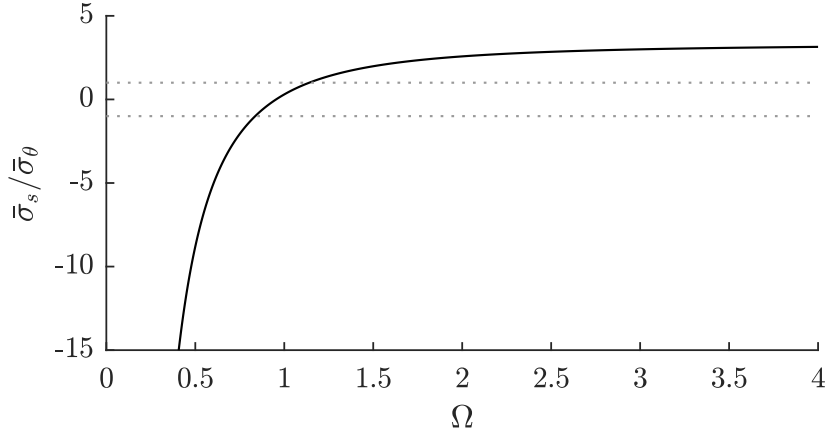


Figure 3: Ratio between the axial and the hoop stress per frequency for $\nu = 0.3$. The ratio approaches $-\infty$ as Ω approaches zero. The dashed lines indicate when $\bar{\sigma}_s/\bar{\sigma}_\theta = \pm 1$.

is reasonable to assume a uni-axial stress state at this low frequency range. However, when the ring frequency is approached, the hoop stress is no longer negligible compared to the axial component, and a bi-axial state needs to be considered. For simplicity, a uni-axial stress state will be used in the following,

180 therefore restricting the applicability of the model to $\Omega < 0.5$.

The membrane equations (4) are split into three expressions relating the axial displacement, \bar{u} , the total axial strain, ε , and the axial stress $\bar{\sigma}_s$, yielding:

$$\frac{\partial^2 \bar{u}}{\partial \tau^2} = (1 - \nu^2) \frac{\partial \bar{\sigma}_s}{\partial s}, \quad (9a)$$

$$\varepsilon = \frac{\partial \bar{u}}{\partial s}, \quad (9b)$$

$$\bar{\sigma}_s = \varepsilon + \frac{\partial^2 \bar{\sigma}_s}{\partial s^2} - \frac{\partial^2 \bar{\sigma}_s}{\partial \tau^2}. \quad (9c)$$

These three relations are the equilibrium, kinematic and constitutive equations for a linear elastic axi-symmetric membrane, respectively. By discarding the time derivative in the latter expression, the corrected rod theory, i.e. Eq. (5), is retrieved. Moreover, the total axial strain is split into an elastic and a plastic part: $\varepsilon = \varepsilon_e + \varepsilon_p$. After inserting this expression and transforming back to

dimensional quantities, the equations for the corrected rod, including physically non-linear behaviour, read

$$\rho \frac{\partial^2 u}{\partial t^2} = \frac{\partial \sigma}{\partial x}, \quad (10a)$$

$$\varepsilon = \frac{\partial u}{\partial x}, \quad (10b)$$

$$\sigma = E(\varepsilon - \varepsilon_p) + \underbrace{R^2 \frac{\partial^2 \sigma}{\partial x^2}}_{\text{Correction}}, \quad (10c)$$

in which σ denotes the axial stress. This set of equations closely resembles the model equations presented in the paper by DeVault [10] based on the Rayleigh-Love rod theory. For a solid cylindrical rod with radius R , the expression for the axial stress becomes:

$$\sigma = E(\varepsilon - \varepsilon_p) + \underbrace{\frac{1}{2} \nu^2 R^2 \frac{\partial^2 \sigma}{\partial x^2}}_{\text{RL correction}}. \quad (11)$$

185 It is important to note that the stress state in the Rayleigh-Love rod theory is always uni-axial, i.e. independent of frequency, whereas the stress state for the corrected rod is essentially bi-axial for $\Omega > 0.5$.

Since the system of equations (10) is not yet complete, auxiliary relations for the plastic axial strain, $\varepsilon_p(x, t)$, are needed. Assuming uni-axial plasticity with linear isotropic hardening, one obtains [25]:

$$\frac{\partial \varepsilon_p}{\partial t} = \gamma \text{sign}(\sigma), \quad (12a)$$

$$\frac{\partial \alpha}{\partial t} = \gamma, \quad (12b)$$

$$f(\sigma, \alpha) = |\sigma| - (\sigma_y + K\alpha), \quad (12c)$$

$$\gamma \geq 0, \quad f(\sigma, \alpha) \leq 0, \quad \gamma f(\sigma, \alpha) = 0, \quad (12d)$$

$$\gamma \frac{\partial f(\sigma, \alpha)}{\partial t} = 0 \quad \text{if } f(\sigma, \alpha) = 0, \quad (12e)$$

where γ is the magnitude of the plastic flow rate, α the hardening parameter, K the plastic modulus, $f(\sigma, \alpha)$ the yield function, and σ_y the yield stress of the material. This set of equations forms the basis for the discussion in Section 3.

190

2.4. Hammer force

To represent the hammer impact, an axial force $F(t)$ is introduced at the pile head positioned at $x = 0$. This force can be measured during an experiment or modelled using a hammer-pile model, e.g. the model of Deeks and Randolph [26]. At $x = L$, the boundary condition is dependent on the soil characteristics. In this paper, however, the main interest lies in the shape of the stress wave as it first passes the measurement location, since this information is sufficient to conclude whether plastic deformation occurred at the pile head. Thus, a simulation stops before the stress wave reflected by the soil reaches the sensor. Therefore, the boundary condition at $x = L$ is of no importance for the discussion hereafter, and zero displacement, i.e. $u = 0$, is prescribed.

3. Method to quantify plastic deformation

When plastic deformations are considered, stress above the local yield limit can no longer propagate, affecting the shape of the original stress pulse. Due to this limit, a plateau in the stress signal appears. Furthermore, a part of the energy contained in the stress wave is used to permanently deform the structure. These two aspects are the basis for the method to detect and quantify plastic deformation in this paper.

The effect of the non-linear material behaviour on the shape of the stress wave is elaborated by considering simulated time signals of the axial strain in a small-diameter pile. Table 1 presents the considered parameters; and a sketch of the pile is shown in Figure 1. An elastic and an elasto-plastic simulation of the wave propagation in the pile are performed with the same force signal applied at $x = 0$, which is presented in the inset graph in Figure 4.

Figure 4 shows the strain signals at $x = 3.0$ m resulting from the two simulations. In the elastic case, the shape of the signal is identical to that of the force signal. However, in the elasto-plastic case, a plateau in the strain is visible, indicating that plastic deformation has occurred. Thus, by comparing the measured strain signal with the expected strain computed on the basis of the elastic

Table 1: Parameters for the simulations of a small-diameter steel monopile.

Parameter	Value
R	0.25 m
h	0.010 m
L	50 m
a	3.0 m
E	210 GPa
K	4.2 GPa
ν	0.3
ρ	7750 kg/m ³
σ_y	235 MPa

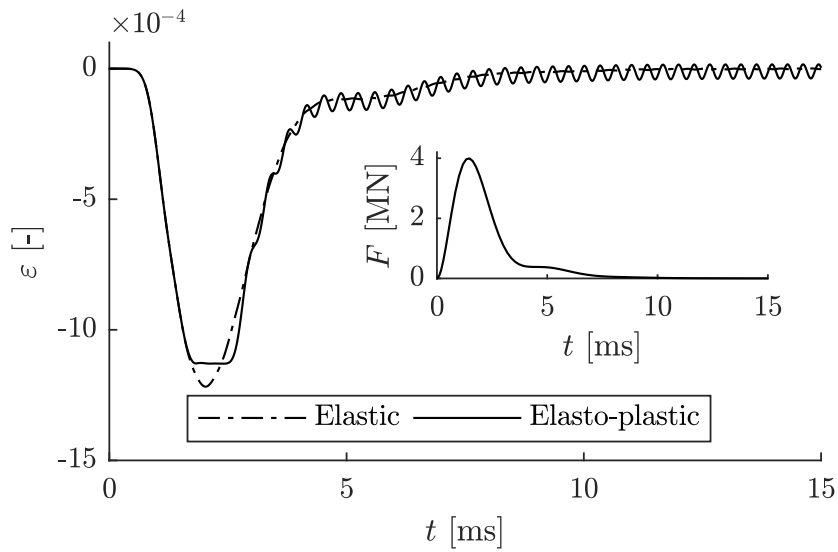


Figure 4: Strain signals at $x = 3.0$ m for an elastic and an elasto-plastic simulation of a small-diameter pile; the inset graph shows the force signal used in both cases.

220 model of the structure, one can reach some preliminary conclusions regarding the possible development of plastic deformation at the pile head caused by the hammer impact.

To quantify this deformation, the following elementary energy balance is considered:

$$E_0 = E_w + E_p + E_{\text{loss}}, \quad (13)$$

225 in which E_0 denotes the input energy of the hammer, E_w the energy associated with the wave energy flux through the considered cross-section, E_p the energy lost in work to plastically deform the material, and E_{loss} the remaining losses, e.g. losses in sound radiation and attenuation. Each contribution to the energy balance is elaborated below.

230 The input energy E_0 is determined by a hammer model or by scaling the linear response of a low energy impact. The energy E_w that passed through a cross-section is defined as the integral of the energy flux over a given time interval from $t = t_0$ to $t = t_1$:

$$E_w = \int_{t=t_0}^{t=t_1} Fv \, dt. \quad (14)$$

Using the relations $F = A\sigma$, $\sigma = E\varepsilon$ and $v = \sigma/\sqrt{E\rho}$, this integral can be 235 rewritten in terms of the axial strain ε , as follows:

$$E_w = \frac{AE^2}{\sqrt{E\rho}} \int_{t=t_0}^{t=t_1} \varepsilon^2 \, dt, \quad (15)$$

in which A is the area of the cross-section.

The plastic work E_p is equal to the integral over time of the mechanical dissipation as defined in [25]:

$$E_p = \int \mathcal{D}_{\text{mech}} \, dt = A \int_{t=t_0}^{t=t_1} \int_{x=0}^{x=a} \left(\sigma \frac{\partial \varepsilon_p}{\partial t} - K\alpha \frac{\partial \alpha}{\partial t} \right) dx \, dt. \quad (16)$$

Using the auxiliary equations (12) and the fact that $\sigma \text{sign}(\sigma) = |\sigma|$, the plastic 240 work is rewritten as

$$E_p = A \int_{t=t_0}^{t=t_1} \int_{x=0}^{x=a} (\gamma [|\sigma| - \sigma_y - K\alpha] + \gamma \sigma_y) dx \, dt. \quad (17)$$

Since the term between square brackets is the yield function $f(\sigma, \alpha)$ and the auxiliary relations require that $\gamma f(\sigma, \alpha) = 0$, the expression reduces to

$$E_p = A\sigma_y \int_{t=t_0}^{t=t_1} \int_{x=0}^{x=a} \gamma \, dx \, dt. \quad (18)$$

The double integral of the plastic flow rate is an indicator of the amount of plastic deformation between the impact and sensor location; and it is henceforth referred to as a single quantity u_p : the permanent axial displacement. With this
 245 new quantity defined, the expression for the plastic work reduces to

$$E_p = A\sigma_y u_p. \quad (19)$$

Of the remaining losses in the pile, E_{loss} , the discussion in [27] showed that the energy in the acoustic radiation is negligibly for sensors positioned above the seabed. Therefore, provided that the other loss mechanisms are also small,
 250 E_{loss} can be altogether neglected for the first-order estimation of the amount of plasticity. By reordering the energy balance, u_p is expressed as

$$u_p = \frac{E_0 - E_w}{A\sigma_y}. \quad (20)$$

Eq. (20) gives a simple relation to quantify the plastic deformation caused by an impact load based on a single strain measurement at a certain distance from the impact point. Naturally, this expression will give an upper bound estimation of
 255 the expected plastic strain as E_{loss} is assumed equal to zero.

4. Lab-scale experiment

As an example, the proposed method is applied to the lab experiments of Kolsky and Douch [12]. In their paper, a solid cylindrical copper specimen of length L_0 with initial velocity v_0 impacts a stationary solid cylindrical copper
 260 rod with length L_1 . The experiment was repeated with increasing initial velocities to show the effect of the yield limit on the shape of the induced stress pulse in the rod. Figure 5 shows a schematic of the experimental set-up. Both the specimen and the rod have the same radius R ; it is listed in Table 2, together with the other dimensions and material properties. In this specific set-up,

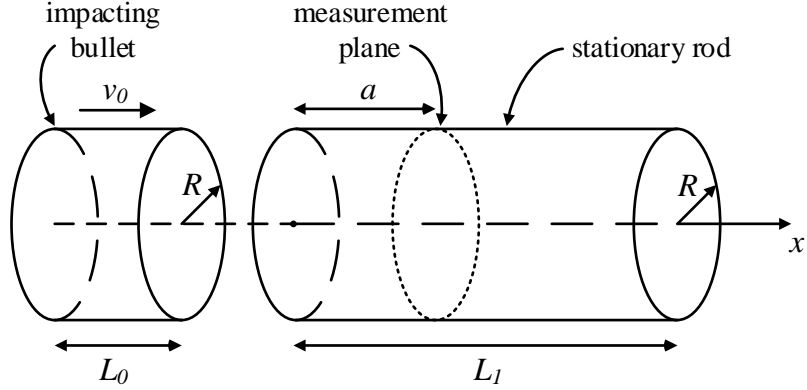


Figure 5: The modelled set-up of the lab-scale experiment of Kolsky and Douch [12].

265 the initial energy E_0 follows directly from the initial velocity $v_0 = 14.02$ m/s
 (= 46 ft/s). It reads $E_0 = 1/2mv_0^2 = 36.8$ J, in which m is the specimen's mass
 computed with the density and its volume.

In the original paper, only the oscillograph traces of the stress pulses were
 reported (see Figure 6). Since these traces lack a scale to quantify the actual
 270 stress levels, the measured wave energy E_w is computed by comparing the signals
 for two different impact velocities. Using the response of the low velocity impact,
 $v_0 = 8.53$ m/s (= 28 ft/s), which causes no plastic deformation in the rod,
 the wave energy for the impact of interest ($v_0 = 46$ ft/s) is equal to $E_w =$
 24.6 ± 3.8 J. The uncertainty in the value results from the digitalisation of the
 275 oscillograph traces. By combining these two energies in Eq. (20), the permanent
 axial deformation is estimated at $u_p = 0.20 \pm 0.06$ mm. Note that the entire
 difference between the input energy and the measured wave energy is contributed
 to plastic deformation, as all other losses are assumed to be negligible.

To check whether this estimate is accurate, the high speed impact is also
 280 simulated using the stress wave propagation model introduced in Section 2.3.
 However, because these experiments concern a solid cylinder rather than a thin-
 walled cylindrical shell, the Rayleigh-Love correction term in the stress definition

Table 2: Parameters of the experiment of Kolsky and Douch [12] on copper specimens.

Parameter	Value
L_0	0.1524 m
L_1	1.2192 m
R	9.525 mm
a	0.548 m
E	129.8 GPa
K	1.298 GPa
ν	0.34
ρ	8960 kg/m ³
σ_y	210 MPa

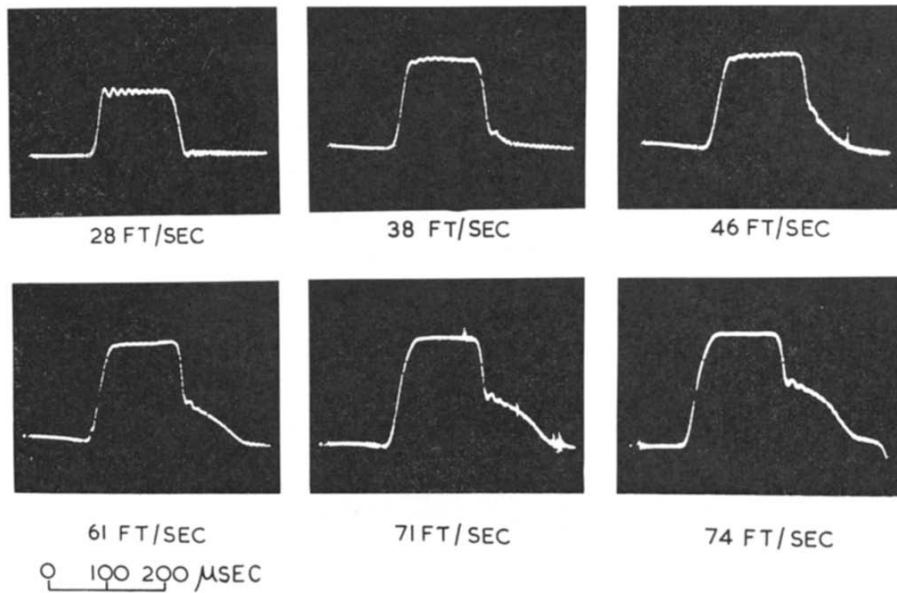


Figure 6: Oscillograph traces of copper on copper impacts—reprint of Fig. 19 from [12], with permission from Elsevier.

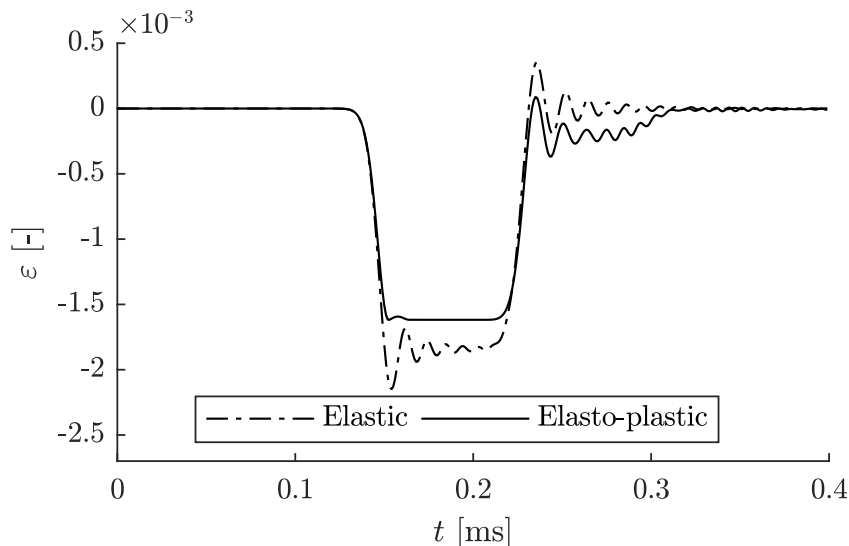


Figure 7: Simulated total strain signals at $x = 0.548$ m for the elastic and the elasto-plastic rod after impact with $v_0 = 14.02$ m/s ($= 46$ ft/s).

is used, i.e. Eq. (11). Two simulations will be compared: a linear elastic simulation, which ignores the yield limit, and a elastic-plastic deformation, which enforces the yield limit. Only the latter simulation includes a loss mechanism, i.e. the plastic deformation; other loss mechanisms are not considered. From the elasto-plastic simulation, it is possible to determine the amount of plastic deformation in the rod, which is then compared to the estimate obtained from the measurements.

For the simulations, the model equations (10) are spatially discretised with the Finite Element Method in FEniCS [28], and an explicit Newmark scheme [29] is used for the time integration. The spatial resolution and time step are $\Delta x = 2.74 \cdot 10^{-3}$ m and $\Delta t = 1.0 \cdot 10^{-7}$ s, respectively. A return mapping algorithm [25] ensures that the auxiliary constitutive equations (12) are all satisfied.

Figure 7 shows the time traces of the total axial strain at the sensor location ($x = 0.548$ m) for the two simulations, while the axial plastic strain along the rod axis of the rod for the elasto-plastic simulation is presented in Figure 8. The latter figure shows that the plastic strain is zero at the sensor location, which

actually means that the total strain in Figure 7 is equal to the elastic strain.

300 In line with the observations by Kolsky and Douch[12], the stress wave at the sensor displays a plateau and a tail for the elasto-plastic case as result of the yield limit. The shape of the tail, however, differs from the experimental one. This difference can attributed to the simple hardening law used in the presented model; in reality, the material response is more complex.

305 The observed changes in the stress wave's shape indicate that plastic deformation occurred, which is also clear from the plastic strain profile presented in Figure 8. With the simulated data, the permanent deformation can be computed in two different ways; either by applying Eq. (20) to the strain signal read from Figure 7, or by integrating the plastic strain along the length of the rod up to the location of the sensor. The latter approach yields:

$$u_p = \int \varepsilon_p dx = 0.131 \text{ mm.} \quad (21)$$

Since no other loss mechanisms are considered in the simulations, the former approach is equivalent to the latter and results in the same value of u_p . However, if one would consider these extra loss mechanisms in the simulations, the predicted strains at the location of the sensor for the elasto-plastic case would 315 have been lower, resulting in a higher value for u_p when Eq. (20) is applied. The plastic strain profile, however, would remain unaffected by these additional loss mechanisms. Given this reasoning and the fact that the predicted plastic deformation u_p is lower than the measured one, it can be concluded that the other loss mechanisms in the experiment are non-negligible. The permanent 320 deformation predicted by the model, however, does confirm that the estimate by the experimental data is an accurate upper bound for the amount of plastic deformation in the rod.

5. Measurements during impact pile driving

Before the same principles can be applied to a large-diameter monopile, the 325 propagation of linear elastic waves in these type of structures is considered more

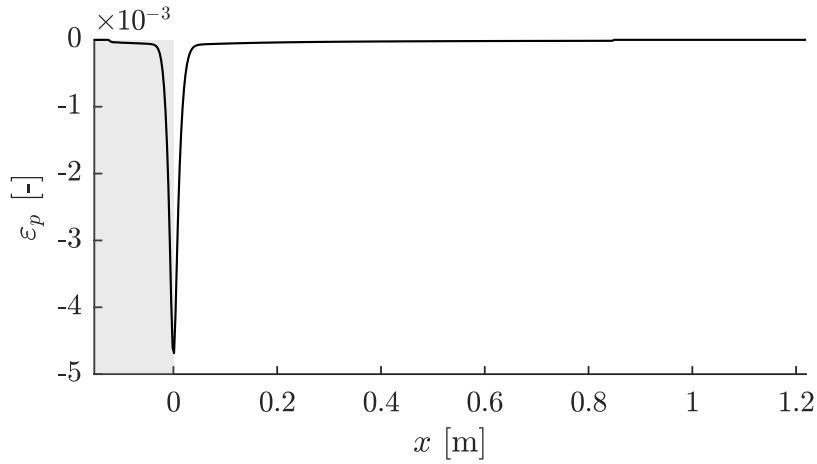


Figure 8: Plastic axial strain from the elasto-plastic simulation along the length of the rod. The shaded grey area is the length of the impacting bullet L_0 .

closely. To this end, data recorded during the installation process of a monopile
 is analysed. The investigated pile has a radius R of 2.5 m; however, piles with
 even larger diameters are currently commissioned [1]. Figure 1 shows a sketch
 of the situation. The pile's dimensions and material properties are listed in
 330 Table 3; with these quantities, the ring frequency is computed as: $f_r = 347$
 Hz. During the driving of the pile, strain levels have been monitored with four
 sensors placed on a ring along the pile's circumference located 9.0 m below the
 pile head. The measured data will first be compared to the results of two linear
 elastic simulations to determine which model is the most accurate for predicting
 335 the stress levels at the sensor location.

As an input for the simulations, the stress signal caused by a hammer impact
 is used; it is shown in Figure 9 with its amplitude spectrum. The frequency
 content reveals that the hammer signal contains some energy at frequencies
 above the ring frequency of the shell. Therefore, it is expected that the corrected
 340 rod theory, Eq. (5), will not accurately reproduce the measured signals. The
 simulations are performed with a finite element discretisation and an explicit
 Newmark scheme; the spatial resolution and time step are $\Delta x = 67.8 \cdot 10^{-3}$ m
 and $\Delta t = 1.0 \cdot 10^{-5}$ s, respectively.

Table 3: Parameters for the installation process of a large-diameter steel monopile.

Parameter	Value
R	2.5 m
h	0.050 m
L	33.9 m
a	9.0 m
E	210 GPa
ν	0.3
ρ	7750 kg/m ³

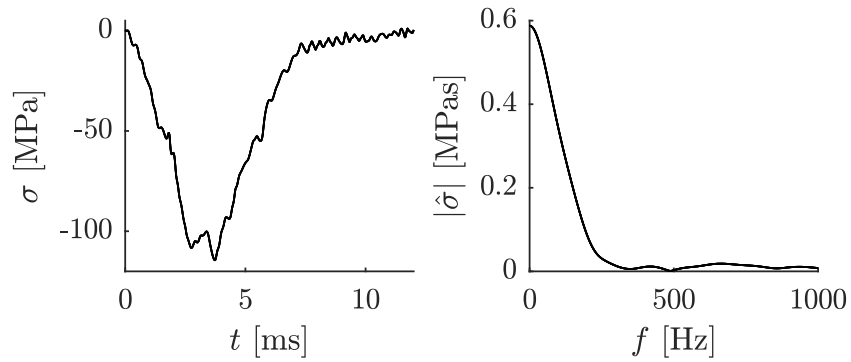


Figure 9: Left, time signal of the stress level induced by the hammer force computed from measurements on the hammer casing; right, amplitude spectrum of this stress signal.

Figure 10 shows the measured stress levels, computed as an average of the
 345 four measured strain signals, together with the results from a linear elastic
 simulation using the membrane theory, i.e. Eq. (4), and the corrected rod
 theory, i.e. Eq.(5). The measured stress signal is relatively smooth for the first
 5 ms, after which oscillations become more pronounced. This behaviour can be
 attributed to a number of factors. First, the input force itself is non-smooth
 350 due to the internal structure of the impact hammer. Stress pulses exerted by
 hammers are characterized by a relatively smooth ascending branch followed
 by several high-frequency oscillations that are caused by the dropping of the
 various smaller internal masses of the hammer on the top of the pile. Second,
 the shell itself is dispersive and, therefore, the excited waves carrying energy at
 355 different frequencies arrive at the location of the sensors at different moments in
 time. Thus, even in the ideal case in which the input force is smooth, dispersion
 effects will tend to distort the original shape of the stress pulse. Third, the pile
 is never positioned totally vertically during installation, and the hammer-pile
 contact is, therefore, non-ideal, resulting in bending of the pile. Waves excited
 360 due to bending of the pile arrive at the location of the sensor at later moments
 in time.

As expected from the frequency restriction of the corrected rod theory, $0 \leq$
 $\Omega < 1 - \nu^2$, the high-frequent oscillations (higher than $f_{\max} = (1 - \nu^2) \cdot f_r =$
 315 Hz) did not propagate, smoothing the signal considerably; nonetheless, the
 365 model can predict the peak stress. The results obtained with the membrane
 theory, however, correctly capture the main features of the measured stress
 pulse, showing the importance of the upper branch of the dispersion relation for
 the stress wave propagation in large-diameter monopiles. For high frequencies
 ($\Omega > 0.5$), the stress ratio, Eq. (8), shows that the hoop stress level has the same
 370 order of magnitude as the axial stress component. From this observation, one
 may safely conclude that a bi-axial stress state is present in a large-diameter
 monopile during pile driving; therefore, the presented method to quantify the
 plastic deformation cannot be applied in that case. An extension of the method
 that includes the bi-axial stress state is needed.

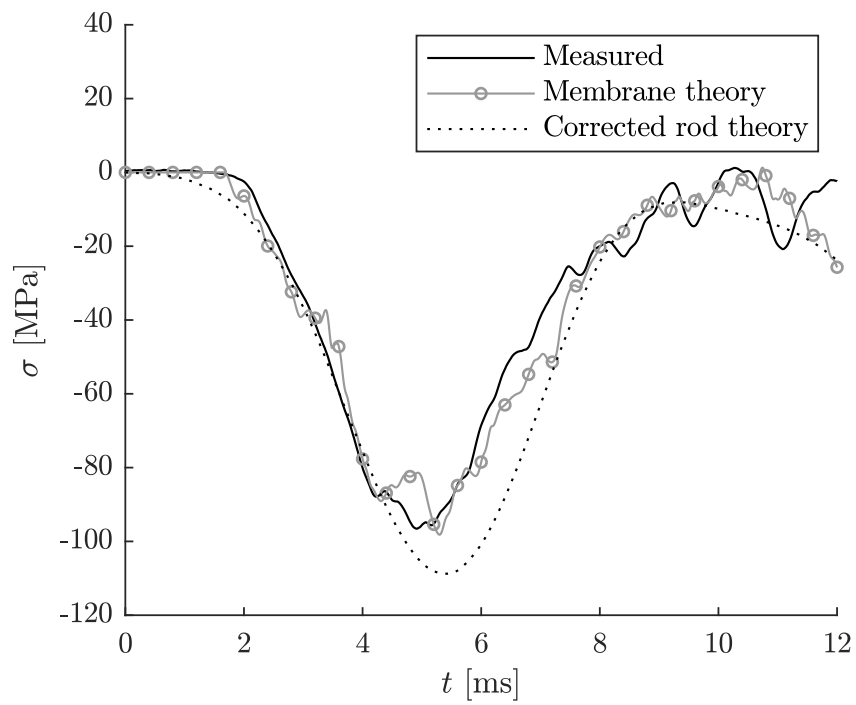


Figure 10: Stress levels at the sensor location ($x = 9.0$ m) for the large-diameter monopile.

375 Although the pile analysed here can be categorised as large-diameter, currently, piles with even larger diameters are being installed. As the ring frequency decreases linearly with increasing radius, one can expect that the hammer impact introduces more energy in the frequency range around the pile's ring frequency, demonstrating the importance of including the effect of wave dispersion
380 in impact driving models for large-diameter monopiles. For piles with small diameters (up to $R = 0.25$ m), however, the energy introduced in the structure by an impact hammer is well below the ring frequency, generating a uni-axial stress state; and the proposed method could readily be applied.

In this specific case, the sensors are positioned relatively far from the pile
385 head; therefore, reflections from the seabed and the pile toe, i.e. stress waves travelling back up the pile, can contaminate the measured strain signal, obscuring the information about plastic deformation contained in the signal. This problem could be resolved by installing the sensors closer to the impact location; or by using strain gauges located at different cross-sections along the pile,
390 enabling one to deduce in which direction different wave components travel. Furthermore, measurements from sensors at multiple levels can be used to localise zones of plastic deformation based on the same principles as the proposed method.

6. Conclusions

395 This study has shown that plastic deformations at the top of a foundation pile can be detected and quantified using non-collocated strain measurements. With an elementary energy balance, an upper bound for the amount of plastic deformation sustained between the impact and sensor location is found by comparing the energy contained in the measured strain pulse to the expected strain
400 signal, which is computed with a linear elastic model of the structure. This paper derives a one-dimensional wave propagation model from thin shell theory to correctly account for stress wave dispersion, since this effect cannot be neglected when the hammer impact introduces energy around the ring frequency

of the shell.

405 The proposed method to quantify plastic deformation is based on a uni-axial stress state, and it gives an adequate estimation when it is applied to a lab-scale experiment, where this stress state is valid. However, data of the installation a large-diameter monopile clearly showed that only the full membrane theory was able to reproduce the measurements, meaning that a bi-axial stress state is developed in the shell. The proposed quantification method can therefore not be applied directly to this situation, although generalising it for a bi-axial stress state is quite straightforward. In contrast, impact driving generates a uni-axial stress state in small-diameter piles, allowing the use of the method during the installation of these piles.

415 A potential problem for the method are the stress waves reflected from the seabed, since they contaminated the measured strain signal. This can be resolved either by using strain sensors at more locations further down the pile, providing sufficient information to compensate for this effect, or by ensuring that the sensor is as close as possible to the pile head. As the method is based on routine strain measurements, applying it during the driving process of small-diameter monopiles is simple; and it can give a valuable insight into the state of the support structure after installation.

Acknowledgements

425 This research is part of the EUROS programme, which is supported by NWO domain Applied and Engineering Sciences and partly funded by the Dutch Ministry of Economic Affairs. The authors would like to thank IHC-IQIP for providing the measurement data of the impact pile driving.

References

- 430 [1] WindEurope, The European offshore wind industry. Key trends and statistics 2016, Tech. rep., WindEurope (2017).

- [2] E. A. L. Smith, Pile-driving analysis by the wave equation, American Society of Civil Engineers Transactions 127 (1962) 1145–1193.
- [3] F. Rausche, M. Nagy, S. Webster, L. Liang, CAPWAP and Refined Wave Equation Analyses for Driveability Predictions and Capacity Assessment of Offshore Pile Installations, in: ASME 2009 28th International Conference on Ocean, Offshore and Arctic Engineering, American Society of Mechanical Engineers, 2009, pp. 375–383.
- [4] A. Tsouvalas, A. V. Metrikine, A semi-analytical model for the prediction of underwater noise from offshore pile driving, Journal of Sound and Vibration 332 (13) (2013) 3232–3257. doi:10.1016/j.jsv.2013.01.026.
- [5] P. G. Reinhall, P. H. Dahl, Underwater Mach wave radiation from impact pile driving: Theory and observation, The Journal of the Acoustical Society of America 130 (3) (2011) 1209–1216. doi:10.1121/1.3614540.
- [6] M. E. Mabsout, J. L. Tassoulas, A finite element model for the simulation of pile driving, International Journal for Numerical Methods in Engineering 37 (2) (1994) 257–278.
- [7] P. C. Meijers, A. Tsouvalas, A. V. Metrikine, The Effect of Stress Wave Dispersion on the Drivability Analysis of Large-Diameter Monopiles, Procedia Engineering 199 (2017) 2390–2395. doi:10.1016/j.proeng.2017.09.272.
- [8] G. Taylor, The use of flat-ended projectiles for determining dynamic yield stress I. Theoretical considerations, Proc. R. Soc. Lond. A 194 (1038) (1948) 289–299. doi:10.1098/rspa.1948.0081.
- [9] T. Von Karman, P. Duwez, The propagation of plastic deformation in solids, Journal of Applied Physics 21 (10) (1950) 987–994.
- [10] G. P. DeVault, The effect of lateral inertia on the propagation of plastic strain in a cylindrical rod, Journal of the Mechanics and Physics of Solids 13 (2) (1965) 55–68. doi:10.1016/0022-5096(65)90020-7.

- [11] J. H. Shea, Propagation of Plastic Strain Pulses in Cylindrical Lead Bars, *Journal of Applied Physics* 39 (8) (1968) 4004–4011. doi:10.1063/1.1656889.
- 460
- [12] H. Kolsky, L. S. Douch, Experimental studies in plastic wave propagation, *Journal of the Mechanics and Physics of Solids* 10 (3) (1962) 195–223. doi:10.1016/0022-5096(62)90038-8.
- [13] A. Khayer Dastjerdi, R. Naghdabadi, J. Arghavani, An energy-based approach for analysis of dynamic plastic deformation of metals, *International Journal of Mechanical Sciences* 66 (2013) 94–100. doi:10.1016/j.ijmecsci.2012.10.011.
- 465
- [14] W. Ren, H. Mingbao, H. Zhuping, Y. Qingchun, An experimental study on the dynamic axial plastic buckling of cylindrical shells, *International Journal of Impact Engineering* 1 (3) (1983) 249–256. doi:10.1016/0734-743X(83)90021-0.
- 470
- [15] K. Murase, N. Jones, The Variation of Modes in the Dynamic Axial Plastic Buckling of Circular Tubes, in: N. Gupta (Ed.), *Plasticity and Impact Mechanics*, Wiley Eastern Limited, New Delhi, 1993, pp. 222–237.
- [16] Ü. Lepik, Bifurcation analysis of elastic–plastic cylindrical shells, *International Journal of Non-Linear Mechanics* 34 (2) (1999) 299–311. doi:10.1016/S0020-7462(98)00032-8.
- 475
- [17] D. Karagiozova, M. Alves, N. Jones, Inertia effects in axisymmetrically deformed cylindrical shells under axial impact, *International Journal of Impact Engineering* 24 (10) (2000) 1083–1115. doi:10.1016/S0734-743X(00)00028-2.
- 480
- [18] D. Karagiozova, N. Jones, Influence of stress waves on the dynamic progressive and dynamic plastic buckling of cylindrical shells, *International Journal of Solids and Structures* 38 (38) (2001) 6723–6749. doi:10.1016/S0020-7683(01)00111-1.
- 485

- [19] D. Karagiozova, N. Jones, Dynamic elastic–plastic buckling of circular cylindrical shells under axial impact, *International Journal of Solids and Structures* 37 (14) (2000) 2005–2034. doi:10.1016/S0020-7683(98)00343-6.
- 490 [20] J. E. Greenspon, Vibrations of Thick and Thin Cylindrical Shells Surrounded by Water, *The Journal of the Acoustical Society of America* 33 (10) (1961) 1321–1328. doi:10.1121/1.1908429.
- [21] A. W. Leissa, *Vibration of Shells*, Acoustical Society of America New York, 1993.
- 495 [22] C. H. Hodges, J. Power, J. Woodhouse, The use of the sonogram in structural acoustics and an application to the vibrations of cylindrical shells, *Journal of Sound and Vibration* 101 (2) (1985) 203–218. doi:10.1016/S0022-460X(85)81216-5.
- [23] W. F. Bozich, *The Vibration and Buckling Characteristics of Cylindrical Shells Under Axial Load and External Pressure*, Tech. rep. (1967).
- 500 [24] K. F. Graff, *Wave Motion in Elastic Solids*, Dover Publications, Mineola, N. Y., 1991.
- [25] J. C. Simo, T. J. Hughes, *Computational Inelasticity*, Vol. 7, Springer Science & Business Media, 2006.
- 505 [26] A. J. Deeks, M. F. Randolph, Analytical modelling of hammer impact for pile driving, *International Journal for Numerical and Analytical Methods in Geomechanics* 17 (5) (1993) 279–302.
- [27] A. Tsouvalas, A. V. Metrikine, A three-dimensional vibroacoustic model for the prediction of underwater noise from offshore pile driving, *Journal of Sound and Vibration* 333 (8) (2014) 2283–2311. doi:10.1016/j.jsv.2013.11.045.
- 510

[28] A. Logg, K.-A. Mardal, G. N. Wells, et al., Automated Solution of Differential Equations by the Finite Element Method, Springer, 2012.

[29] N. M. Newmark, A Method of Computation for Structural Dynamics, Journal of the Engineering Mechanics Division 85 (No. EM 3) (1959) 67–94.

515